Analyst

PAPER

View Article Online
View Journal | View Issue

Cite this: *Analyst*, 2015, **140**, 2493

Rapid biodiagnostic *ex vivo* imaging at 1 μm pixel resolution with thermal source FTIR FPA

C. R. Findlay,[a] R. Wiens,[a] M. Rak,[a] J. Sedlmair,[b] C. J. Hirschmugl,[b] Jason Morrison,[c] C. J. Mundy,[d] M. Kansiz[e] and K. M. Gough*[a]

Received 30th October 2014,
Accepted 7th January 2015

DOI: 10.1039/c4an01982b

www.rsc.org/analyst

A recent upgrade to the optics configuration of a thermal source FTIR microscope equipped with a focal plane array detector has enabled rapid acquisition of high magnification spectrochemical images, in transmission, with an effective geometric pixel size of ~1 × 1 μm^2 at the sample plane. Examples, including standard imaging targets for scale and accuracy, as well as biomedical tissues and microorganisms, have been imaged with the new system and contrasted with data acquired at normal magnification and with a high magnification multi-beam synchrotron instrument. With this optics upgrade, one can now conduct rapid biodiagnostic *ex vivo* tissue imaging in-house, with images collected over larger areas, in less time (minutes) and with comparable quality and resolution to the best synchrotron source FTIR imaging capabilities.

Introduction

FTIR imaging is now a well-established analytical method for obtaining spatially resolved spectral and spatial information simultaneously in the micron-scale domain and has been applied across many different application areas, from polymer science to biomedical imaging.[1] Progress in pushing the diffraction-limited spatial resolution performance of FTIR imaging systems has been led by synchrotron based systems.[2]

We describe a novel method of magnification enhancement, that couples high numerical aperture (NA) objectives and new magnification optics in an FTIR microscope with a thermal source spectrometer to yield FTIR imaging capabilities that are comparable to the highest synchrotron source imaging capability yet demonstrated.[2] The new optics permit high magnification imaging on the order of 1 μm^2 per pixel, with a Focal Plane Array (FPA). Without these optics, the normal magnification imaging yields an effective geometric pixel area of 5.5 × 5.5 μm^2 at the sample plane. This implementation, for the first time, yields spectra with signal to noise ratio (SNR) comparable to that of synchrotron source FTIR imaging, on relatively fast time-scales (~6 minutes per FPA tile). There is no need for recourse to noise reduction post-processing algorithms. The design maintains a substantial and usable 21 mm working distance and is compatible with full sized FPA (128 × 128). The signal quality is sufficient to enable sub-micron spatial resolution imaging in Attenuated Total Reflection (ATR) mode, with a Ge crystal as Internal Reflection Element (IRE), yielding a 0.22 × 0.22 μm^2 pixelation, all using a single objective.

We present here the first examples of this instrumentation applied to standard targets to test precision and accuracy, and to biological samples: cryosectioned, post-mortem tissue from Alzheimer disease brain and cryopreserved, single cell organisms (Arctic sea ice diatoms). Data are contrasted with images acquired with normal magnification on the thermal source system and with a multi-beam synchrotron-based FTIR imaging system (IRENI, Synchrotron Radiation Center, WI).

Taken together, our results demonstrate that, compared to standard magnification, significant added spectral and spatial detail is observed with the new optics. In comparison to the highest magnification achieved with a synchrotron based system (IRENI),[2,3] equivalent or better detail is obtained, especially in the information rich fingerprint region, below 1800 cm^{-1}, where the stable illumination from the thermal source proves to give better, more consistent baselines to permit better image analysis overall.

Experimental

FTIR instrumentation

Thermal source FTIR spectrochemical imaging was done with an Agilent Technologies Cary 670 FTIR spectrometer coupled

[a]*Department of Chemistry, University of Manitoba, Winnipeg MB, Canada R3T2N2. E-mail: Kathleen.Gough@umanitoba.ca*
[b]*Physics Department, University of Wisconsin-Milwaukee, WI, USA*
[c]*Department of Biosystems Engineering, University of Manitoba, Winnipeg MB, Canada R3T2N2*
[d]*Centre for Earth Observation Science, Department of Environment and Geography, University of Manitoba, Winnipeg MB, R3 T 2N2, Canada*
[e]*Agilent Technologies Pty Ltd, 679 Springvale Rd, Mulgrave, VIC. 3170, Australia*

to a Cary 620 FTIR microscope equipped with a 64 × 64 FPA mercury cadmium telluride (MCT) detector (University of Manitoba) or with a 128 × 128 FPA (Agilent Technologies, Mulgrave). Additional software-controlled hardware and optics, including a 15×, 0.62 NA objective with 21 mm working distance, were supplied by Agilent, yielding a 1.1 μm pixel edge, instead of the normal magnification (5.5 μm pixel edge), in transmission mode. The new design implemented in the high magnification thermal source instrument places additional magnification (5× increase) optics in front of the FPA. Through automated software, the user can change the configuration from pixel resolution of ~1.1 μm to the standard 5.5 μm pixel size by changing optics within the microscope body (proprietary to Agilent Technologies, patent pending), rather than by changing the objective. This novel design preserves the full 21 mm working distance of the 0.62 NA, 15× objective, enabling the use of other accessories such as ATR. Magnification was further increased by 4× with the ATR accessory, though additional practical limitations affect the achievable effective sample magnification at the detector.

Comparison images have been acquired with the thermal source instrument operated under normal magnification, and with wide-field, multi-beam synchrotron source illumination.[2] The latter had a Bruker Hyperion 3000 FTIR microscope, with a 74×, 0.65 NA, 1 mm working distance objective and 15×, 0.65 NA condenser, yielding an effective geometrical area of 0.54 × 0.54 μm^2 per pixel on the 128 × 128 FPA detector, in transmission mode (IRENI). The specifications of that system have been described in detail elsewhere.[2,3] The SRC facility was decommissioned in March 2014, but it has been possible to perform direct comparisons on 1951 US Air Force (USAF) targets and preserved cryosectioned tissue. Freshly acquired diatoms from spring 2014 are compared to diatoms imaged prior to the closure of SRC.

Materials

Standardization targets. A high resolution (groups 1–9) 1951 USAF target (Ronchi rulings of chrome on glass) was used to test resolving power under transmission (groups 6 and 7) and ATR (groups 8 and 9) operating conditions. A standard resolution (groups 1–7) 1951 USAF target was also used in some tests.

Human post-mortem tissue. Unfixed, frozen hippocampal tissue came from a 91 year old female patient with advanced AD (Braak 6).[4] The tissue was obtained from the Netherlands Brain Bank (NBB), at the Netherlands Institute for Neuroscience, Amsterdam; a written informed consent for a brain autopsy, and the use of the material and clinical information for research purposes, had been obtained by the NBB. The sample was cryosectioned at −20 °C; 8 μm thick sections were placed on BaF_2 windows for IR imaging. Plaque location and identity were confirmed with Congo red staining of sections serial to those imaged with FTIR (data not shown).

Diatoms. Samples were collected from a landfast first-year ice site in Dease Strait near Cambridge Bay, NU, Canada (69° 1.622′N; 105° 19.699′W) under the umbrella of the Ice Covered Ecosystem – CAMbridge bay Process Studies (ICE-CAMPS) project in March 2014. Multiple ice cores were extracted using a 9 cm diameter Mark II Coring System (Kovacs Enterprises) from sites with average snow depth of 3–7 cm and ice thickness of 200 cm. The bottom 0–5 cm sections of each core were pooled into a single isothermal container, diluted with 0.2 μm filtered seawater (FSW) at a volume ratio of approximately 3 : 1 (FSW : ice melt) to minimize osmotic shock of the microbial community while melting in the dark over an 18 h period.[5] A 20 mL aliquot was filtered onto polycarbonate filters (3 μm pore size, Sterlitech Corp., USA). These were folded, sealed in aluminium foil and stored in a portable −80 °C freezer on-site, in order to preserve biochemical integrity.[6] At the University of Manitoba, samples were transferred to an in-house −80 °C freezer. For IR imaging, diatoms were released from filter paper onto a BaF_2 window with a few drops of MilliQ water, and rinsed once with a few drops of MilliQ water that was wicked away with tissue to reduce formation of salt crystals while minimizing osmotic shock. The samples were dried in the dark, at room temperature inside a chamber with SiO_2 desiccant overnight and imaged at once, or stored at 6 °C and imaged within 48 hours.

Methods

For data acquired in transmission mode in the University of Manitoba laboratory, images were obtained as a sum of 128 scans ratioed to 512 background scans, at 4 cm^{-1} spectral resolution, with zero filling set to 2. The standard resolution USAF target (groups 1–7) was imaged in transmission, in the IR-transparent region above 2200 cm^{-1}; it was also imaged with normal and high-magnification mode ATR. Biological samples mounted on BaF_2 windows were imaged in transmission mode.

Images of standard and high resolution USAF targets were acquired in the Agilent laboratories (Mulgrave AU) on a similar instrument equipped with a 128 × 128 FPA. To assess the maximum practical spatial resolution possible with the new optics, Groups 8 and 9 were imaged with the slide-on ATR accessory and Ge IRE. The contact region corresponds to an area of ~70 × 70 μm^2 at normal magnification and ~14 × 14 μm^2 with the high magnification optics engaged.

For external comparison, the identical areas in the brain tissue samples were imaged in transmission with the wide-field, multi-beam synchrotron source illumination with a geometric pixel resolution of 0.54 × 0.54 μm^2 on the 128 × 128 FPA detector (IRENI). Importantly, this system provided the highest commercially available NA optics, achieving the highest diffraction-limited resolution possible for transmission experiments. At IRENI, all mid-IR wavelengths were sampled at diffraction-limited resolution.

Results and discussion

The performance of the new optical configuration was assessed in transmission mode by imaging through the glass

of a standard and high resolution USAF targets and through biological samples mounted on BaF_2 windows. The samples were selected to represent highly contrasting challenges in imaging, from standard resolution targets, to typical tissue sections, to isolated unicellular organisms with irregular surfaces and contrasting sub-cellular content. To test ultimate effective pixelation limits, a slide-on ATR with Ge crystal was used on an AFT to image elements of groups 8 and 9. To the best of our knowledge, this is the first example of ATR imaging wherein the oversampled pixel size, relative to the shortest wavelengths, compressed in the Ge Internal Reflection Element (IRE) to one quarter of wavelength in air, is within the 4 to 5× oversampling regime. This meets the oversampling requirements across the mid-IR spectrum, as the pioneering work at IRENI has taught us.

Much has already been written about spatial resolution in FTIR imaging,[7–10] and the fundamentals are well established from other imaging modalities such as the comparison between confocal and widefield fluorescence imaging.[11] With each technical innovation, the known factors must be considered and tested against standardized objects, typically the 1951 USAF targets, and with real objects. It is important to keep in mind that resolution cannot be precisely defined, and that the main goal should be to create valid contrast between key elements in the processed images.

Both Rayleigh (eqn (1)) and Sparrow (eqn (2)) criteria are often used to define resolution in microscopy, where minimum resolvable separation is given by the formulae:

$$d = \frac{0.61\lambda}{\mathrm{NA}} \quad (1)$$

$$d = \frac{0.47\lambda}{\mathrm{NA}} \quad (2)$$

in which λ = wavelength; NA is numerical aperture = $n \sin\theta$; n = refractive index of the medium and θ = 1/2 cone angle (outer ray) of light captured by the objective. The total system magnification is given by (native detector size)/(sample pixel size). The objective alone is only one factor in calculating the total magnification. The key to achieving a particular spatial resolution lies in the pixel size at the sample, which may be effectively altered by additional magnification optics between the sample and the detector plane, as has been done with the Agilent system.

1951 USAF target images

Transmission. Contrast is created between 100% transmission, through glass and 0% transmission through the chrome bars, above 2100 cm^{-1}. Pixelation and noise affect the achievable resolution; in principle, at least 8 samples (pixels) must be acquired across a bar, or 12 across two bars, with an acceptable contrast minimum between bars.[11] Since glass is transparent down to 2100 cm^{-1}, standard and high resolution USAF targets (Ronchi rulings of chrome on glass) were examined in transmission first with normal optics engaged, then with the new high magnification optics. The results are shown in Fig. 1. The normal optics with the Agilent FPA provide effective pixelation of 5.5 × 5.5 μm^2, comparable to other arrays and to many standard single pixel, raster-scan synchrotron end-stations that operate without an array. With the new optics engaged, the FPA pixelation should theoretically become 1.1 × 1.1 μm^2. Groups 6 and 7 on the AFT provide line pairs of 64 to 228 mm^{-1}, with individual line widths ranging from 7.81 to 2.19 μm (Fig. 1A). In order to assess the false color images in raw pixel format, the image files were exported to Matlab. The transmittance image through the USAF target is shown in Fig. 1B, C imaged in normal and high magnification mode, respectively. Plots of the raw transmittance at 2500 cm^{-1}, extracted from individual pixels in a continuous line through the vertical chrome bars of elements 1, 2 and 3, again for normal and high magnification, Fig. 1D and E, respectively.

For the purposes of comparison with similar tests of resolution in FTIR,[7–10] we consider the Rayleigh criterion first. Within this paradigm, two bars in the target are deemed to be laterally resolved if the maximum in one bar coincides with the first zero crossing of the adjacent bar, resulting in a difference of 26.4% in transmitted light. Microscopists also use the Sparrow criterion, which defines a lower limit below which there is zero contrast between two adjacent bars.[11] Contrast is evaluated from difference in $\%T$ at the peaks and valleys across the target, normalized by their sum, which in principle should be 100%. If the effective pixel size is less than the wavelength-dependent separation required to create contrast, then the objects may be deemed to be resolved.

Attenuated total reflection. The working distance with the 15× 0.62 NA Agilent objective is 21 mm, and thus easily accommodates the slide-on Ge IRE (NA 3.44). With the Ge IRE and the high magnification optics engaged, additional magnification is obtained, surpassing even that achieved with the IRENI system. Unfortunately, the working distance in the latter was too small to accommodate an IRE. The USAF target was imaged again under these conditions and the results are shown in Fig. 2. The visible image for Group 9 (Fig. 2A) shows the region corresponding to a single 128 × 128 FPA tile processed as $\%T$ at 2500 cm^{-1} (Fig. 2B). Because one half of the ATR optic is used for illumination and the other half to transmit the light to the detector, the resolution is biased in favour of vertical bars. This is immediately apparent in the contrast achievable between the vertical bars of elements 1, 2 and 3, compared to the unresolved horizontal bars of the same dimension (Fig. 2B). Similarly the numeral 1 on the right hand side is almost completely distinguishable, while only the vertical strokes of the numerals 2 and 3 are apparent. The values of $\%T$ at 2500 cm^{-1} for the pixels that cross the vertical bars of the three elements of Group 9 are shown in Fig. 2C. All values are within the Rayleigh criterion for resolution, even for element 3, with 780 nm bars.

A false colour image was created by integrating the area under the Si–O stretching band located around 1000 cm^{-1} (Fig. 2D). Typical absorbance spectra from glass and chrome (Fig. 2E) show that there is sufficient contrast to distinguish the glass against the vertical chrome bars. This may be under-

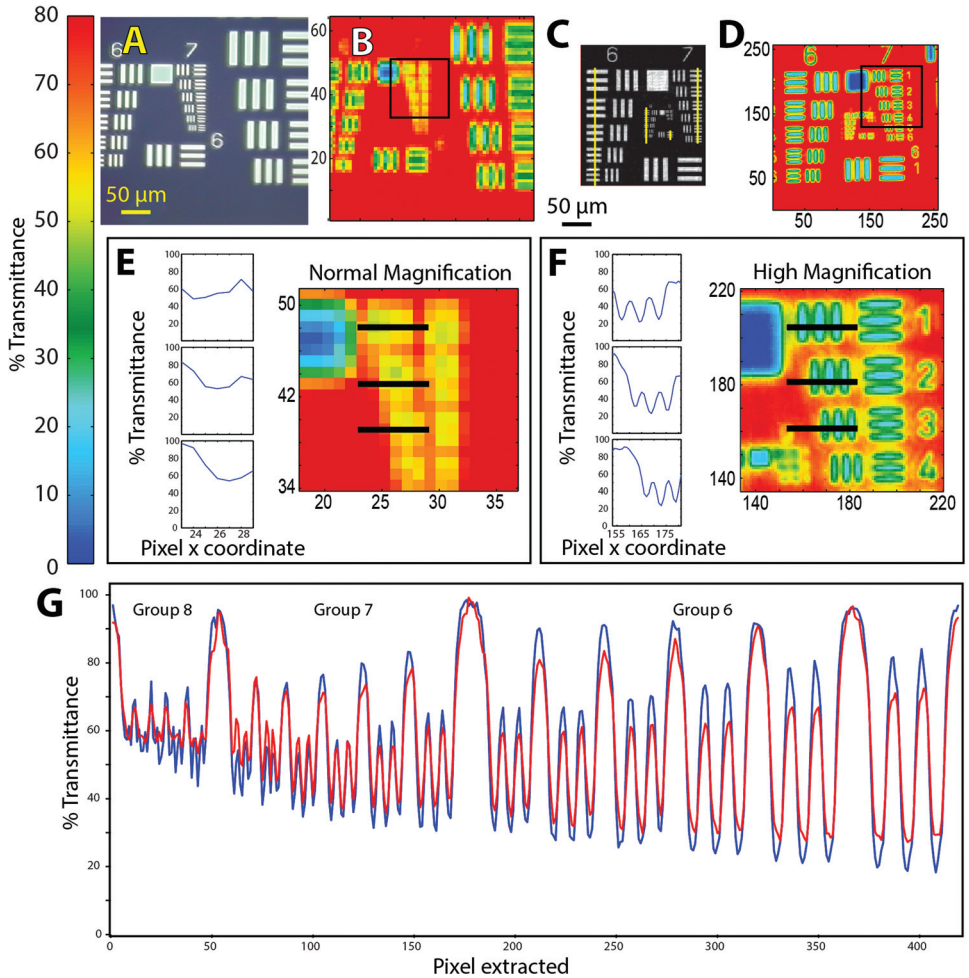

Fig. 1 FTIR of 1951 USAF targets (chrome on glass) imaged in transmission at normal and high magnification. (a) Visible image of target 1. (b) Normal magnification (5.5 × 5.5 μm^2 per pixel) transmission mode FTIR image, single tile (64 × 64 FPA), processed as %*T* at 2500 cm^{-1}. (c) Visible image of target 2. (d) High magnification (1.1 × 1.1 μm^2 pixel) FTIR image processed as %*T* at 2500 cm^{-1}, 2 × 2 tiles (128 × 128 FPA). (e) Normal magnification and (f) High magnification FTIR images of boxed areas in (b) and (c). Line graphs show %*T* at adjacent pixels located along horizontal black lines through elements 1, 2 and 3 of group 7 in each FTIR image. (g) Line graph shows %*T* at 3500 cm^{-1} (blue trace) and 2500 cm^{-1} (red trace), extracted pixel by pixel from high magnification FTIR image (d). Location of pixels is indicated by vertical yellow lines through all elements of groups 6, 7 and 8, drawn on the visible image (c) for clarity.

stood in terms of the Sparrow limit of 0.136 μm pixel resolution for this wavelength and NA. The image is of greater interest for practical applications. Discrimination between an IR absorbing material (glass) and the IR-reflective chrome bars is relatively easy. The practical applications of imaging real samples under high magnification will involve non-reproducible scatter within a sample, such as biological tissue, overlapping bands from complex materials, and noise. These applications are considered in the next section.

Cryosectioned brain tissue

Cryosectioned brain tissue images are taken from our on-going research with FTIR spectrochemical imaging to identify cellular and sub-cellular features in Alzheimer's disease (AD) brain tissue.[12] AD presents a major, growing health concern worldwide; the few approved therapies provide small symptomatic relief; efforts to halt, reverse or prevent AD are so far unsuccessful. None of the several postulated hypotheses adequately explain AD, possibly because the processes identified are temporally "downstream" from direct causative factors that occur years, even decades, prior to appearance of clinical symptoms. In this research, we analyze FTIR spectrochemical images of unfixed, snap-frozen, desiccated brain tissue sections from human AD autopsy cases and transgenic AD mouse models. Given the multifactorial origins of AD, we are focused on the temporal evolution and molecular composition of senile plaques and neurofibrillary tangles (the hallmarks of diseased brain) and on the detection of features that may be overlooked or altered by histopathological and immunohistochemical methods.[6]

We have already noted the additional insight possible with higher magnification imaging that permits sub-cellular resolution.[13] The upgraded optics provide spectral data of the same or superior quality, and nearly comparable effective pixel size.

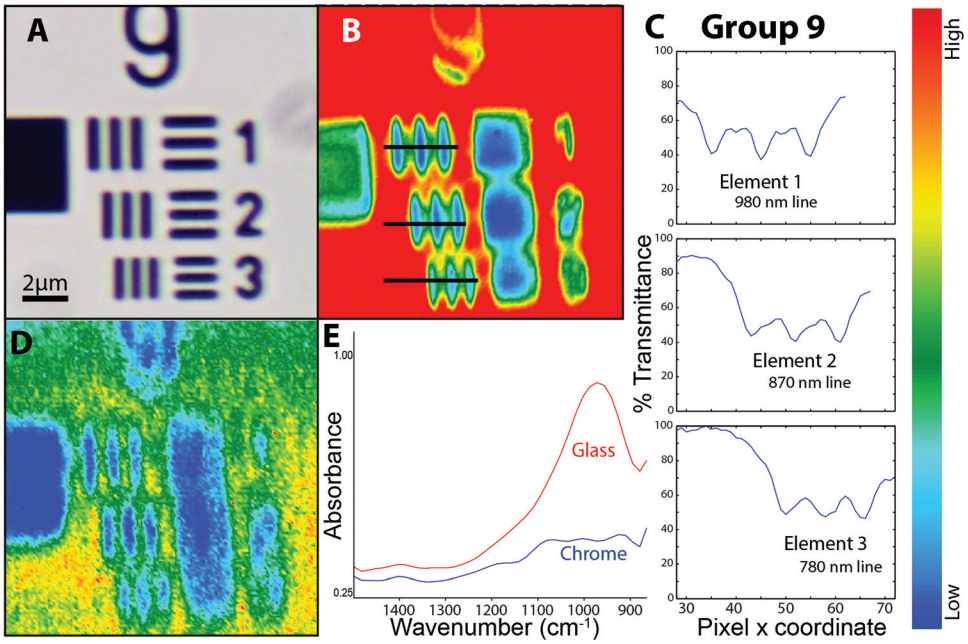

Fig. 2 FTIR–ATR images of elements in group 9 of the high spatial resolution 1951 USAF target. (a) Visible image of elements in group 9. (b) FTIR–ATR image (128 × 128 FPA) at high magnification (nominal 0.25 × 0.25 μm^2 per pixel) processed as %*T* though glass at 3500 cm^{-1}. (c) Line plot of %*T* at adjacent pixels extracted from image, across each element, shows that contrast exceeds sparrow criterion. Pixels extracted at locations shown in (b) as horizontal black lines. (d) FTIR–ATR image processed on integrated intensity of Si–O band. (e) Absorbance spectra taken from a single pixel on glass (red) and a single pixel on chrome bar (blue) showing Si–O band.

A dense core plaque from human autopsy brain was imaged at IRENI prior to the facility closure. The desiccated sample was stored at 4 °C and later imaged with the Agilent FTIR microscope, using normal and high magnification optics (Fig. 3).

The plaque in this image is located in the *stratum moleculare* of the hippocampus, a region characterized by some denser white matter tracts and a few capillaries. Neuronal cell bodies are few, being located mainly in the pyramidal layer and in the dentate gyrus. Visible images of the plaque region are shown at 10× and 40× (Fig. 3A, left and right, respectively); white boxes outline the areas imaged at the three magnifications. The Amide I band shows the presence of β-sheet conformation (1630 cm^{-1}) in each of the spectra (Fig. 3B) which have been extracted from the same location within the plaque core. The α-helix-β-sheet doublet is poorly resolved at the lowest magnification (5.5 μm pixel edge), presumably because the area sampled includes a broader swath of material and incorporates less of the actual dense core. Whether this is because the core itself is poorly transmitting cannot be ascertained, and is not significant. More important is the comparison between the new high magnification optics with thermal source and the spectrum obtained with the multi-beam synchrotron source. The Amide I profiles are essentially identical, showing that the core composition is fairly uniform at 1 μm resolution. The baseline at the longest wavelength is slightly better with the thermal source, offering the potential for image analysis with long wavelength bands. The OH, NH and CH stretch regions appear to be nearly identical. The NH stretch is more pronounced in the two high magnification spectra (thermal and synchrotron sources), as they isolate a purer sample of plaque core.

We have used our standard protocols to create false colour images of plaque core, membrane lipid and creatine crystals (Fig. 3C, left to right) from low to high magnification. At normal magnification (Fig. 3C, top row, left) the dense core plaque is registered at a few pixels, but not strongly, owing to the poorer spectral definition described above. Membrane lipid, comprised mainly of long chain fatty acid esters, is marked by intensity of the symmetric CH_2 stretch band at 2850 cm^{-1} and is seen throughout the region, as expected for the molecular layer (Fig. 3C, top row, center). There is increased membrane signature in the plaque vicinity, as has been observed in our previous studies of human and mouse model plaques.[14,15] Creatine crystals dot the surface, again a typical phenomenon particularly for aged brain. The precise location of the crystals is an accident of the freeze-thaw process; the abundance may be related to disease progress as well as to age.[13–15] Since the creatine molecule is an amino acid derivative, it possesses several amide-like bands that result in spectral false positives for plaque. The actual location of creatine crystals is visualized from the intensity of sharp bands at 1405, 1395 and 1310 cm^{-1}, Fig. 3C, top row, right. There is no creatine directly associated with the plaque itself.

The corresponding high magnification thermal source and the synchrotron source images are shown in the middle and bottom rows of Fig. 3C. There is no difference in the plaque outline or shape between these two, and also no difference in creatine (absent from this area). There seems to be some

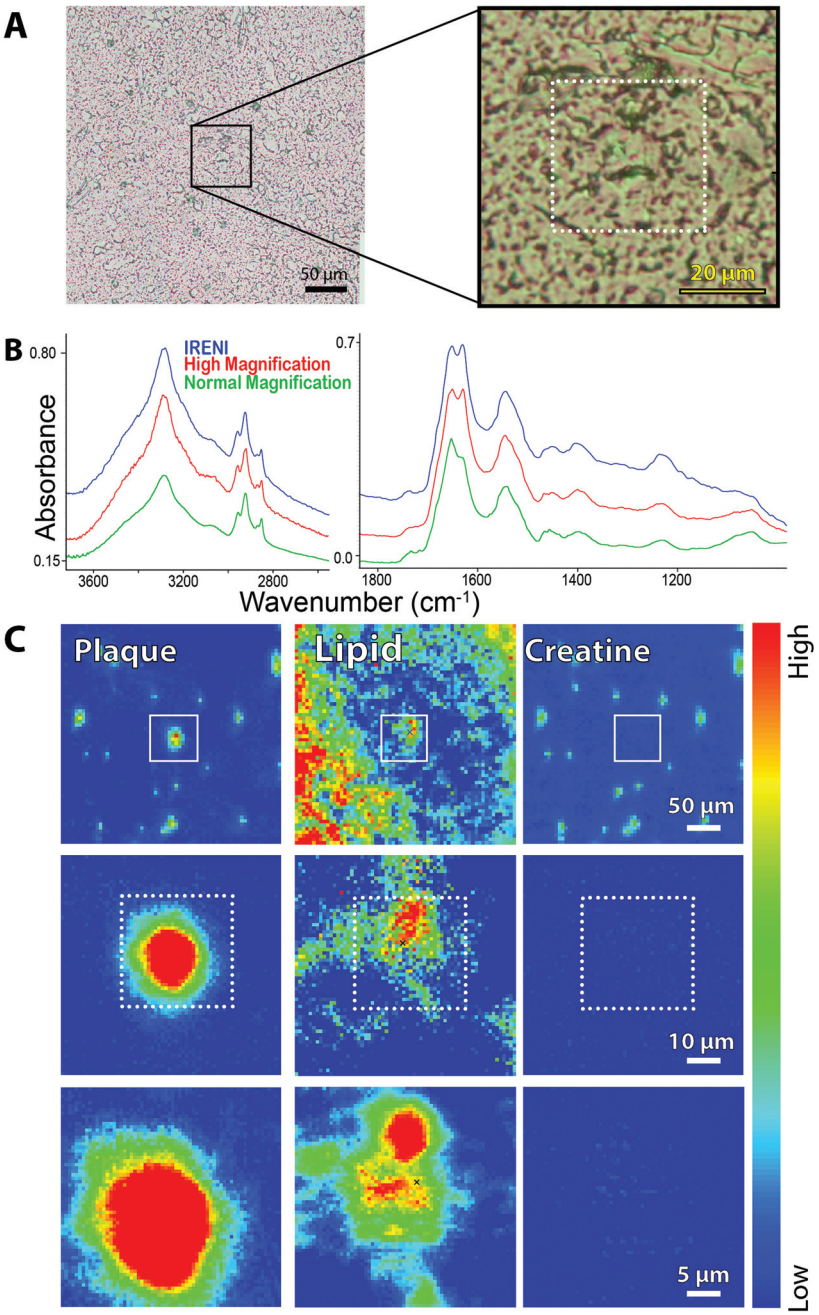

Fig. 3 FTIR spectrochemical images of amyloid plaque in post-mortem brain from an ad case. (a) Photo (left) shows region imaged at normal magnification (64 × 64 FPA, 5.5 × 5.5 μm^2 per pixel). region outlined by black box is expanded (right) to show area imaged with high magnification agilent optics and (dashed white box) area imaged with ireni. (b) Individual spectra extracted from same location in plaque core from ireni image (blue), agilent high magnification (red), and agilent normal magnification (green) showing oh/nh/ch stretch (left) and fingerprint (right) regions. Spectra are displayed on common scale, offset for clarity, here and in Fig. 4–6. (c) False colour FTIR spectrochemical images processed to show left plaque core (1620–1630 cm^{-1}; baseline 1610–1642 cm^{-1}), (centre) lipid membrane (2844–2857 cm^{-1}; baseline 2895–3001 cm^{-1}), and (right) creatine crystals (1300–1311 cm^{-1}; baseline 1289–1322 cm^{-1}) from agilent normal magnification (top row), agilent high magnification (middle), and ireni (bottom).

improvement in the display of the symmetric CH_2 distribution in the IRENI image, showing that at the shortest wavelengths that system was superior. However, the conclusions enabled with the IRENI images remain clearly evident, primarily the observation that the dense core plaques are enveloped and permeated with lipid membranous material.

A region containing two dense core plaques was imaged as two separate FPA tiles at IRENI and in a single FPA tile with the new high magnification optics. The visible image, selected spectra and false colour images processed for plaque, membrane lipid and creatine are shown in Fig. 4. Once again, the spectral quality is very similar, as is the spectrochemical infor-

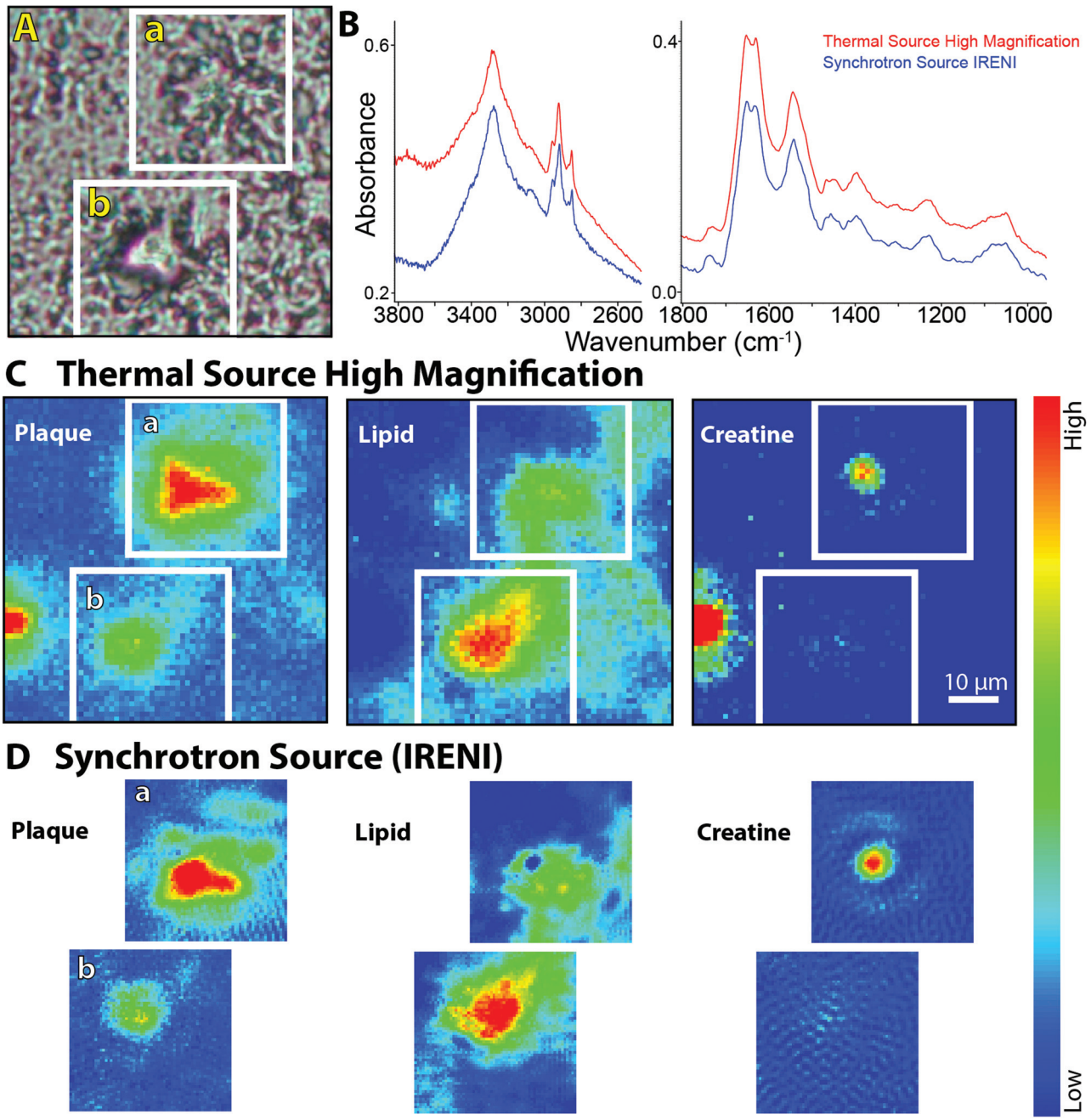

Fig. 4 FTIR spectrochemical images of dense core amyloid plaque in post-mortem brain from an ad case. (a) Visible light image of two dense core plaques showing areas imaged with the agilent high magnification system and with ireni (white boxed outlines). (b) Individual spectra extracted from same location in plaque core from ireni (blue) and agilent high magnification (red) images showing oh/nh/ch stretch (left) and fingerprint (right) spectral regions. (c) Agilent high magnification and (d) Ireni FTIR spectrochemical false colour images processed to show plaque core (left), lipid membrane (centre), and creatine crystals (right), as per Fig. 3c.

mation. We note, of course, that the IRENI pixels were 1/4 the size of the Agilent pixels so, overall, the SNR enabled by the bright synchrotron light would presumably be better. A direct quantitative comparison is not strictly possible since the source intensity in the IRENI image is not known. All three false colour images show nearly identical features. Two small creatine crystals are present in the Agilent high magnification image; one lies outside the region captured in the IRENI images while the other lies on top of the upper plaque. Interestingly, scattering from this small crystal generates a halo of light in the IRENI image and a few fainter pixels in the Agilent image.

There is a trade-off in the IRENI data, also observable in the processed images, arising from a non-reproducible variation in the baseline that is not present in the spectra taken with the thermal source. We have observed this in most of the data

acquired with the IRENI end station. Since the artefact varies from pixel to pixel and tile to tile, these cannot be easily resolved with standard numerical tools. The resultant images exhibit a Moire-like pattern, as seen here in all three processed synchrotron images (Fig. 4D).

Several plaques imaged at IRENI have now been imaged with the upgraded optical system and the results are consistent with the results shown here. In our previous work,[3,6,13,16] we had demonstrated that the unprecedented magnification offered with the IRENI system yielded important new information not obtainable with the 10× larger pixels typical of thermal source FPA systems. Here we find that the images afforded with the new thermal source optics, although the pixels are 2 × 2 larger than those at IRENI, provide essentially the same information with comparable spectral purity, in less time.

Diatoms

We are using FTIR spectrochemical imaging to study the temporal development of the biomass content in Arctic sea ice algal taxa, including *Nitzschia frigida*, *Entomoneis kjellmannii*, *Haslea* spp., and *Fragilariopsis cylindrus*, collected from field samples during the 2014 Arctic spring. Our long term goals in this research are to (1) monitor the relative biomass composition of important ice algae species throughout the spring bloom; (2) identify key environmental factors influencing the temporal development of the ice algae bloom; and (3) evaluate the influence of these factors on the dominant taxa of the ice algae community. The questions posed are critical to understanding potential impacts of climate change on the polar marine ecosystem, while the technical challenges are highly relevant to the development of FTIR spectrochemical imaging. Here we examine normal and high magnification images of representative diatoms and colonies, as obtained with the Agilent system and compare to one sample imaged with the IRENI system.

***Fragilariopsis cylindrus* colony.** Individual diatoms (apical axis: 26 ± 10 μm, transapical axis: 3.0 ± 0.5 μm[17]) readily form colonies by binding along the valve face (Fig. 5A). With the high magnification optics, the outline of the colony can be seen in the false colour image processed on the strong Si–O band around 1075 cm^{-1} that defines the outer frustule (Fig. 5B).

The two chloroplasts in each cell are rich in bioorganic components, as evidenced by the strong protein signal shown as a false colour image (Fig. 5C). Note Fig. 5B and C were processed with ResolutionsPro™ (Agilent Technologies) software, which produces a non-pixelated, blended image. Enlargement of the visible image shows that some of the individual cells in the colony are empty (Fig. 5D, arrows) providing an excellent opportunity to evaluate the achievable spatial resolution. This expanded region corresponds to about 10 × 20 pixels at normal

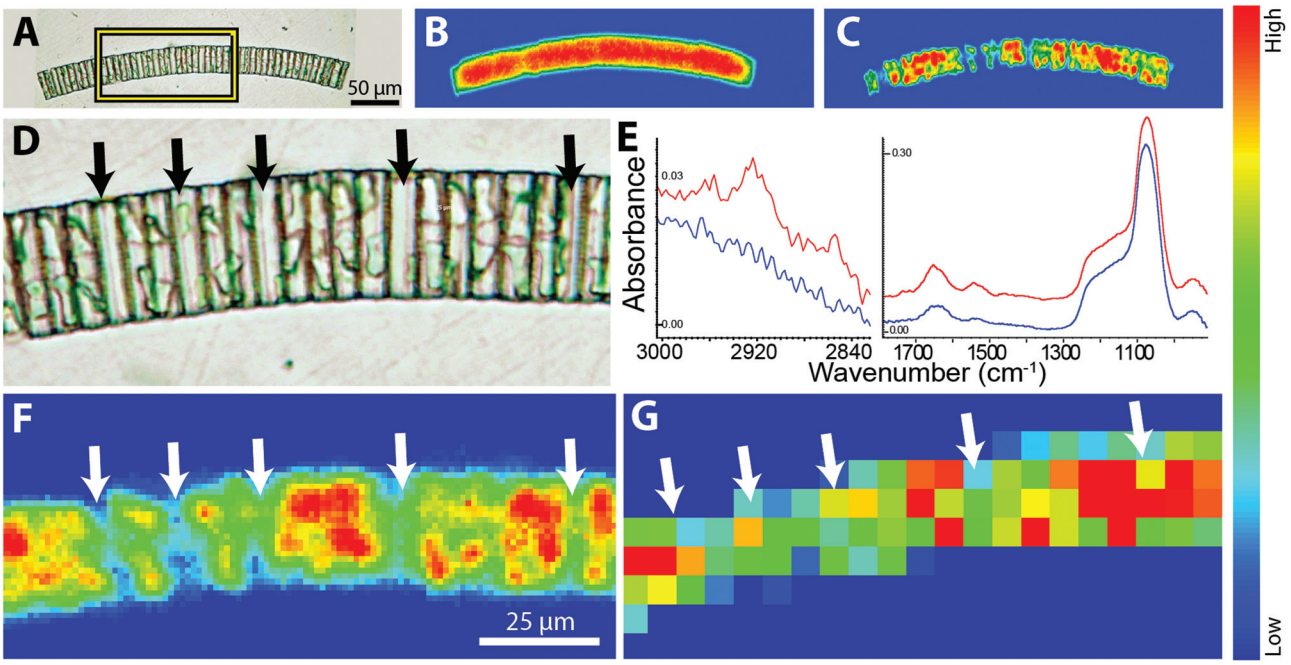

Fig. 5 FTIR spectrochemical images of sea ice diatom colony, *Fragilariopsis cylindrus*, acquired with agilent system using normal and high magnification optics. (a) Visible light photo of colony mounted on baf^2 window. FTIR spectrochemical false colour images at normal magnification processed to show (b) silica frustule, based on integrated intensity of si–o band (1053–1093 cm^{-1}; baseline 1044–1113 cm^{-1}), and (c) chloroplasts, based on integrated intensity of amide i (1663–1685 cm^{-1}; baseline 1493–1764 cm^{-1}). (d) Region outlined by box in (a) expanded to show visible absence of chloroplasts in some cells (black arrows). (e) Individual spectra extracted from putative chloroplast region (red) and visibly empty region (blue) illustrating typical diatom spectral features; chloroplasts show increased protein and lipid. (f) FTIR spectrochemical false colour images showing integrated intensity of amide i band at high magnification and (g) normal magnification, processed in matlab to give true pixelization. Arrows indicate location of visibly empty cells.

magnification, 5.5 μm pixel edge. The mosaic has been reprocessed in MatLab to reveal the pixelation of the data at normal and high magnification. Individual Absorbance spectra selected from protein-rich (red) and protein-deficient (blue) regions are displayed in Fig. 5E, and show the excellent SNR obtained with the high magnification optics, despite the low total absorbance. Protein is detected even in the absence of the obvious chloroplast shapes. This is ascribed to cytoplasm; additionally, there will be some protein associated with the biogenic silica frustule; no lipid is detectable here. The strongest protein signal clearly corresponds to the location of the residual chloroplasts in this colony (Fig. 5F). This pixelated MatLab output is compared to the same region imaged at normal magnification and also processed in MatLab (Fig. 5G). The variation in protein intensity crudely follows that of the high magnification image but lacks any meaningful definition.

Two diatoms, imaged with the new high magnification optics, are compared to a diatom imaged with the IRENI system (Fig. 6) to assess image and spectral quality. Single cells of *E. kjellmannii* (girdle view, Fig. 6A, ResolutionsPro™ software), and *Haslea* spp., possibly *H. crucigeroides*, (valve view, Fig. 6B, OPUS™ software, Bruker Optics) are resolved in remarkable detail, as is the *Nitzschia* spp. (Fig. 6C, imaged at IRENI in 2013).

The outer frustule of each is marked by the presence of the Si–O band at 1075 cm^{-1}. Given the long wavelength of this band, the spatial resolution is at its poorest, yet the outline is distinct. In contrast, the image created by integrating in the SiO–H stretch region (Fig. 6A; 3246 cm^{-1}) of the *E. kjellmanni*

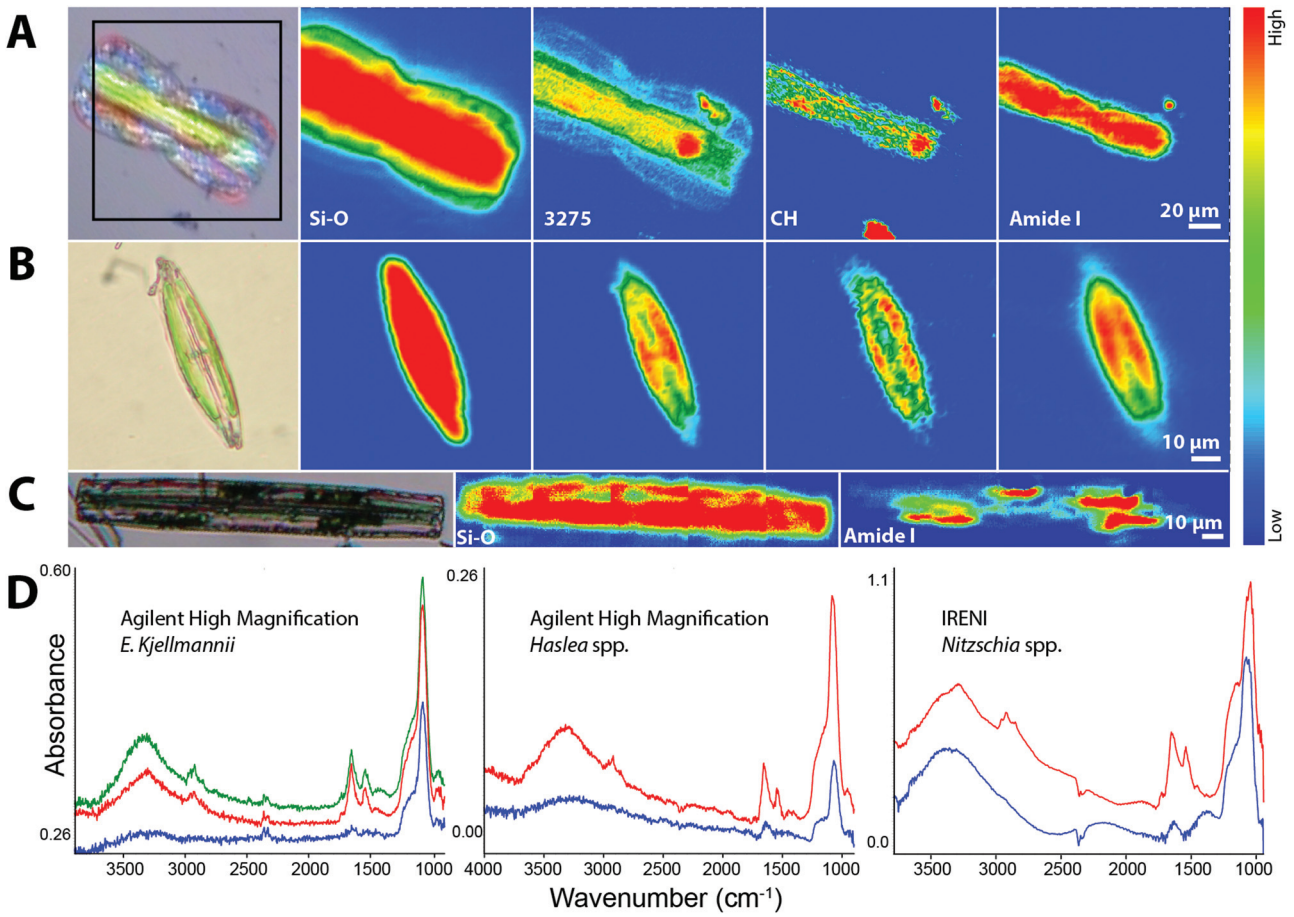

Fig. 6 FTIR spectrochemical images of three arctic sea ice diatoms, processed on integrated intensities of relevant bands to show sub-cellular features. (a) *Entomoneis kjellmanni* imaged with agilent high magnification optics, 2 × 2 tiles, 64 × 64 FPA. From left to right, visible image and FTIR spectrochemical images showing silica frustule (Si–O 1086–1053 cm^{-1}; baseline 975–1313 cm^{-1}), cingula (Sio–H at 3275, 3240–3324 cm^{-1}; baseline 2560–3755 cm^{-1}), lipid storage (ch stretch region, 2848–2970 cm^{-1}; baseline 2598–3718 cm^{-1}) and chloroplast (amide i, 1610–1685 cm^{-1}; baseline 1488–1806 cm^{-1}). (b) *Haslea* spp. imaged as single tile, 64 × 64 FPA, agilent high magnification optics, and processed as per Fig. 6a. Left to right: visible image, and FTIR spectrochemical images showing silica frustule (Si–O), distinctive cruciform (Sio–H at 3275), lipid (ch stretch region) and chloroplast (amide i). (c) *Nitzschia* spp. imaged at ireni (1 × 5 tiles, centre 64 × 64 pixels of the 128 × 128 FPA). Left to right: visible image and FTIR spectrochemical images showing silica frustule (Si–O, 1000–1100 cm^{-1}) and chloroplasts (amide i, 1620–1675 cm^{-1}). (d) Individual spectra extracted from each image. Left: *E. kjellmanni* spectra from visibly empty outer frustule (blue spectrum), chloroplast (red spectrum) and putative lipid storage body (green spectrum). Middle: *Haslea* spp. spectra from empty outer frustule region (blue spectrum) and from chloroplast (red spectrum). Right: *Nitzschia* spp. spectra from empty outer frustule region (blue spectrum) and from chloroplast (red spectrum). All false colour images are rendered in resolutions pro (agilent) or opus (ireni), not pixelated.

cell reveals multiple subtle details in the structure. Striations running the length of the apical axis are clearly associated with the silica bands of the girdle (cingulum), while a large circular organelle is revealed towards the lower left end of the chloroplast region. The cingula are also formed of silica, though originally templated by protein scaffolds (cingulins).[18] These mature cingula are marked by the presence of SiOH groups, indicating some bonding with water has occurred.[19] The chloroplasts do not fill the cell, ending about 20 μm from the lower right end in this view. A relatively-lipid rich organelle at this end (Fig. 6A, CH band) stands out in contrast to the protein content, which is distributed evenly throughout the chloroplast, (Fig. 6A amide band) suggesting that organelle is a nutrient storage body. Since the CH-stretch modes are well-oversampled under the new optics, the dimension of the organelle can be safely approximated at ~15 microns diameter, most likely corresponding to a lipid storage vesicle. Neither the cingula nor the lipid organelle could be identified in the normal magnification image (data not shown).

The *Haslea* spp. (Fig. 6B) is distinguished by the small transapical cross located at centre of the cell. The Si–O signal reaches a maximum at this location, but the image created in the integrated intensity of the band does not match the cruciform morphology. Interestingly, the 3274 cm^{-1} band does produce a matching false colour image, though neither the weaker CH nor the Amide I images do so. The latter two are closely associated with the physical extent of the green chloroplasts which nearly fill the cell in this view. The *trans*-apical cross must include mature hydrated silica. A small amount of protein is still detectable in the transparent region at the bottom but is much lower than in the main body.

The Synchrotron Radiation Center was closed in March 2014, thus it was not possible to obtain comparable images of these diatoms with the IRENI system. A large *Nitzschia* spp. previously imaged in a series of 5 FPA tiles at IRENI is shown in Fig. 6C. As with the diatoms above, integration of the Si–O band shows the full outline of the frustule while the Amide I band shows the concentrated protein in the chloroplasts.

Spectra extracted from each of the images are compared in Fig. 6D. Since the species are all different, we have selected spectra corresponding to a maximum and minimum of protein in each. For the *E. kjellmanni*, a third spectrum was extracted from the centre of the lipid-rich organelle. All diatoms exhibit similar spectral profiles. The outer region of the frustule is almost completely devoid of protein and lipid, though a small amount of protein is seen, presumably associated with the structural wall composition. The signal for lipid-rich region in the *E. kjellmanni* is about 40% stronger than in the surroundings.

The diatoms imaged with the Agilent are smaller than that imaged at IRENI, and conditions differed, so only qualitative comparisons can be made. The integrated absorbance across the midIR spectrum scales roughly with size of the diatom, *i.e. Nitzschia* > *E. kjellmanni* > *Haslea*. Despite the fact that the pixels in Fig. 6C are 1/4 the dimension of those in 6A and 6B, the absorbance maximum is strongest in the IRENI data and SNR is better (Fig. 6D, right) as could be expected given the brilliance of the synchrotron source. However, the non-reproducible variation in the baseline limits the interpretation, compared to the spectra taken with the thermal source. The irregular sinusoidal undulations in the IRENI spectra could arise from scatter, given that the shape and dimension of the diatom is on the order of the mid-IR wavelengths. However such variations were also apparent in regions well away from the diatom where no signal existed, and were also discernible in blank images. As speculated above, these might arise from variations in the multiple overlapped synchrotron beams, exacerbated by the slow but steady decay in the source intensity.

Comparison of advantages and disadvantages

Theoretical considerations for oversampling have been discussed by Carr *et al.*[20] With IRENI's 0.54 um pixel size, there was significant, even severe, oversampling across the fingerprint region, limiting the field of view and resulting in reduced energy at the detector. These factors can contribute to slower data collection (co-addition of more scans) for a given measurement area and desired SNR. Despite the very bright source, the expansion of a small synchrotron beam (or beams), to illuminate an FPA area up to 5.1 × 5.1 mm (128 × 128 array) diminishes the synchrotron brilliance advantage. A multi-beam arrangement such as that implemented at IRENI can resolve this, but other practical issues can arise, such as beam movement over time, or decaying signal if not run in continuous top-up mode, and so on. In practice, even with the 12 beams at IRENI, only the 64 × 64 array could be well illuminated, for a 19× smaller field of view than can be achieved with the new high magnification FTIR microscope. Under these conditions, the synchrotron advantage flips to a disadvantage compared to a large thermal source (7 × 5 mm) that provides a better match to the 5.1 × 5.1 mm FPA element.

Excellent SNR is obtained with the high magnification thermal source, without lengthy co-additions of many scans as might be have been anticipated from the 25× smaller field of view. Magnification is achieved with optics placed just ahead of the FPA; moreover, this system employs a thermal source retro-reflector that increases light through the sample by doubling the effective thermal source element area. As a result, while some light is lost relative to normal magnification mode, the amount of lost light is mostly recovered by the use of higher integration times that have little impact on overall data collection times. In practice, we find that the SNR difference between high and normal magnification modes is about 3 to 4× for an equal number of scans (but different integration times). Since integration time has effectively no impact on total data acquisition time, the actual data collection time is very nearly that of the normal magnification and of a synchrotron.

Just as with the development of novel drug therapies, a current goal for FTIR imaging is the development of the technique as a mainstream diagnostic tool. For this to happen, instrumentation and applications must transition from labora-

tory bench to bedside. The data presented here illustrate the potential for rapid, high magnification and wide field spectrochemical imaging with ~1 μm pixel resolution at the sample plane using a thermal source spectrometer. This magnification and SNR quality was previously achieved only with a unique synchrotron installation (IRENI). The advent of this capability represents another important step towards rapid *ex vivo* biodiagnostic imaging.

Conclusions

In this paper, we have presented examples of standard USAF targets and of real objects, imaged in transmission with a thermal source at normal and high magnification, including ATR. Several samples were also imaged on IRENI at the (now-closed) synchrotron source, to assess the performance of the optics upgrade against the best achievable resolution.

With the new imaging optics, we can now conduct rapid biodiagnostic *ex vivo* tissue imaging in-house with the thermal IR source, obtaining images collected over larger areas, in less time (minutes) and with better spectral quality and spatial resolution than the best currently existing synchrotron source FTIR imaging capabilities.

Acknowledgements

The authors thank A. Ciapala, N. Pogorzelec, P. Trokajlo and O. Ojekudo for technical assistance. This research was supported by grants from NSERC Canada (KMG, CJM) and NSF grant no. CHE-1112433 (CJH). The IRENI project (CJH) was supported by NSF grant no. DMR-0619759. The SRC was operated under NSF grant no. DMR-0537588.

Notes and references

1 M. J. Baker, J. Trevisan, P. Bassan, R. Bhargava, H. J. Butler, K. M. Dorling, P. R. Fielden, S. W. Fogarty, N. J. Fullwood, K. A. Heys, C. Hughes, P. Lasch, P. L. Martin-Hirsch, B. Obinaju, G. D. Sockalingum, J. Sulé-Suso, R. J. Strong, M. J. Walsh, B. R. Wood, P. Gardner and F. L. Martin, *Nat. Protoc.*, 2014, **9**, 1771–1791.
2 M. J. Nasse, M. J. Walsh, E. Mattson, R. Reininger, A. Kajdacsy-Balla, V. Macias, R. Bhargava and C. J. Hirschmugl, *Nat. Methods*, 2011, **8**, 413–418.
3 C. J. Hirschmugl and K. M. Gough, *Appl. Spectrosc.*, 2012, **66**, 475–491.
4 H. Braak and E. Braak, *Acta Neuropathol.*, 1991, **82**, 238–259.
5 D. L. Garrison and K. R. Buck, *Polar Biol.*, 1986, **6**, 237–239.
6 C. R. Liao, M. Rak, J. Lund, M. Unger, E. Platt, B. C. Albensi and K. M. Gough, *Analyst*, 2013, **138**, 3991.
7 P. Lasch and D. Naumann, *Biochim. Biophys. Acta*, 2006, **1758**, 814–829.
8 M. J. Nasse, E. C. Mattson, R. Reininger, T. Kubala, S. Janowski, Z. El -Bayyari and C. J. Hirschmugl, *Nucl. Instrum. Methods Phys. Res., Sect A*, 2011, **649**, 172–176.
9 E. C. Mattson, M. Unger, S. Clède, F. Lambert, C. Policar, A. Imtiaz, R. D'Souza and C. J. Hirschmugl, *Analyst*, 2013, **138**, 5610–5618.
10 R. H. Reddy, M. J. Walsh, M. V. Schulmerich, P. S. Carney and R. Bhargava, *Appl. Spectrosc.*, 2013, **67**, 93–105.
11 E. H. K. Stelzer, *J. Microsc.*, 1998, **189**, 15–24.
12 R. A. Sperling, *et al.*, *Alzheimer's & Dementia*, 2011, **7**, 280–292.
13 M. Z. Kastyak-Ibrahim, M. J. Nasse, M. Rak, C. J. Hirschmugl, M. R. Del Belgio, B. C. Albensi and K. M. Gough, *Neuroimage*, 2012, **60**, 376–383.
14 M. Rak, M. R. Del Bigio, S. Mai, D. Westaway and K. M. Gough, *Biopolymers*, 2007, **87**, 207–217.
15 A. Kuzyk, M. Z. Kastyak, V. Agrawal, M. Gallant, G. Sivakumar, M. R. Del Bigio, D. Westaway, R. Julian and K. M. Gough, *J. Biol. Chem.*, 2010, **485**, 31202–31209.
16 E. C. Mattson, M. J. Nasse, M. Rak, K. M. Gough and C. J. Hirschmugl, *Anal. Chem.*, 2012, **84**, 6173–6180.
17 A. O. Cefarelli, M. E. Ferrario, G. O. Almandoz, A. G. Atencio, R. Akselman and M. Vernet, *Polar Biol.*, 2010, **33**, 1463–1484.
18 A. Scheffel, N. Poulsen, S. Shian and N. Kröger, *Proc. Natl. Acad. Sci. U. S. A.*, 2011, **108**, 3175–3180.
19 S. Musić, N. Filipović-Vinceković and L. Sekovanić, *Braz. J. Chem. Eng.*, 2011, **28**, 89–94.
20 G. L. Carr, O. Chubar and P. Dumas, in *Spectrochemical Analysis Using Infrared Multichannel Detectors*, ed. R. Bhargava and I. W. Levin, Wiley-Blackwell, Oxford, 1st edn, 2005, pp. 56–84.